

# Studies of granularity of a hadronic calorimeter for tens-of-TeV jets at a 100 TeV $pp$ collider

C.-H. Yeh<sup>a</sup>, S.V. Chekanov<sup>b</sup>, A.V. Kotwal<sup>c,d</sup>, J. Proudfoot<sup>b</sup>, S. Sen<sup>c</sup>, N.V. Tran<sup>d</sup>, S.-S. Yu<sup>a</sup>

<sup>a</sup> *Department of Physics, National Central University, Chung-Li, Taoyuan City 32001, Taiwan*

<sup>b</sup> *HEP Division, Argonne National Laboratory, 9700 S. Cass Avenue, Argonne, IL 60439, USA.*

<sup>c</sup> *Department of Physics, Duke University, USA*

<sup>d</sup> *Fermi National Accelerator Laboratory*

<sup>e</sup> *Department of Physics, Michigan State University, 220 Trowbridge Road, East Lansing, MI 48824*

---

## Abstract

Jet substructure variables for hadronic jets with transverse momenta in the range from 2.5 TeV to 20 TeV were studied using several designs for spacial size of calorimeter cells. The studies used the full Geant4 simulation of calorimeter response combined with realistic reconstruction of calorimeter clusters used in jet reconstruction. The results indicate that the performance of jet-substructure reconstruction improves with reducing cell sizes.

*Keywords:* multi-TeV physics,  $pp$  collider, future hadron colliders, FCC, SppC

---

## 1. Introduction

Particle collisions at energies beyond those attained at the LHC will lead to many challenges for detector technologies. Future experiments, such as high-energy LHC (HE-LHC), future circular  $pp$  colliders of the European initiative, FCC-hh [1] and the Chinese initiative, SppC [2] will be required to measure high-momentum bosons ( $W$ ,  $Z$ ,  $H$ ) and top quarks with strongly collimated decay products that form jets. Studies of jet substructure can help identify such particles.

The reconstruction of jet substructure variables for collimated jets with transverse momentum above 10 TeV require an appropriate detector design. The most important for reconstruction of such jets are tracking and calorimeter. Recently, a number of studies [3, 4, 5] have been discussed using various fast simulation tools, such as Delphes [6], in which momenta of particles are smeared to mimic detector response.

A major step towards the usage of full Geant4 simulation to verify the granularity requirements for calorimeters was made in [7]. The studies included in this paper have illustrated a significant impact of granularity of electromagnetic (ECAL) and hadronic (HCAL) calorimeters on the shape of hadronic showers calculated using calorimeter

---

*Email addresses:* jwzuzelski18@gmail.com (C.-H. Yeh), chekanov@anl.gov (S.V. Chekanov), ashutosh.kotwal@duke.edu (A.V. Kotwal), proudfoot@anl.gov (J. Proudfoot), sourav.sen@duke.edu (S. Sen), ntran@fnal.gov (N.V. Tran), syu@cern.ch (S.-S. Yu)

hits for two particles separated by some angle. It was concluded that high granularity is essential in resolving two close-by particles for energies above 100 GeV.

This paper makes another step in understanding of this problem in terms of high-level physics quantities typically used in physics analyses. Similar to the studies presented in [7], this paper is based on a full Geant4 simulation with realistic jet reconstruction.

## 2. Simulation of detector response and event reconstruction

The description of the detector and software used for this study is discussed in [7]. We use the SiFCC detector geometry with a software package that represents a versatile environment for simulations of detector performance, testing new technology options, event reconstruction techniques for future 100 TeV colliders.

The GEANT4 (version 10.3) [8] simulation of calorimeter response was complemented with the full reconstruction of calorimeter clusters formed by the Pandora algorithm [9, 10]. Calorimeter clusters were built from calorimeter hits in the ECAL and HCAL after applying the corresponding sampling fractions. No other corrections are applied. Hadronic jets were reconstructed with the FASTJET package [11] using the anti- $k_T$  algorithm [12] with a distance parameter of 0.5.

In the following discussion, we use the simulations of a heavy  $Z'$  boson, a hypothetical gauge boson that arises from extensions of the electroweak symmetry of the Standard Model. The  $Z'$  bosons were simulated with the masses,  $M = 5, 10, 20$  and 40 TeV. The lowest value represents a typical mass that is within the reach of the LHC experiments. The value 40 TeV represents the physics reach for a 100 TeV collider. The  $Z'$  particles are forced to decay to two light-flavor jets ( $q\bar{q}$ ),  $W^+W^-$  or  $t\bar{t}$ , where  $W$  and  $t$  decay hadronically. In all such scenarios, two highly boosted jets are produced, which are typically back-to-back in the laboratory frame. Typical transverse momenta of such jets are  $\simeq M/2$ . The main difference between considered decay types lays in different jet substructure. In the case of the  $q\bar{q}$  decays, jets do not have any internal structure. In the case of  $W^+W^-$ , each jet originates from  $W$ , thus it has two subjects because of the decay  $W \rightarrow q\bar{q}$ . In the case of hadronic top decays, jets have three subjects due to the decay  $t \rightarrow W^+b \rightarrow q\bar{q}b$ . The signal events were generated using the PYTHIA8 generator with the default settings, ignoring interference with SM processes. The event samples used in this paper are available from the HepSim database [13].

## 3. Studies of jet properties

First let us consider several variables that represent jet substructure using different types of calorimeter granularity. The question we want to answer is how close the reconstructed jet substructure variables reflect the input “truth” values that are reconstructed using input particles directly from the PYTHIA8 generator.

In this study we use the jet effective radius and jet splitting scales as benchmark variables to study jet substructure properties for different calorimeter granularity scenarios. The effective radius is the average of the energy weighted radial distance in  $\eta-\phi$  space of jet constituents. Recently, it has been studied for multi-TeV jets in Ref.[14]. A jet  $k_T$  splitting scale [15] is defined as a distance measure used to form jets by the

59  $k_T$  recombination algorithm [16, 17]. This variable has been studied by ATLAS [18],  
60 and more recently in the context of 100 TeV physics [14]. The splitting scale is defined  
61 as  $\sqrt{d_{12}} = \min(p_T^1, p_T^2) \times \delta R_{12}$  [18] at the final stage of the  $k_T$  clustering, where two  
62 subjets are merged into the final one.

63 Figures 1 and 2 show the distributions of the jet effective radius and jet splitting  
64 scale for different jet transverse momenta and HCAL granularities. The reconstructed-  
65 level distributions significantly disagree with the distributions reconstructed using truth-  
66 level particles. The distribution reconstructed with the cell sizes 1 cm×1 cm are clos-  
67 est to the truth-level variables. The distributions reconstructed using the cell size of  
68 20 cm×20 cm, which is similar to the nuclear interaction length of  $Fe$  ( $\lambda_I \simeq 17$  cm) the  
69 SiFCC calorimeter [7], show the largest discrepancy with the truth-level variables. Note  
70 that, in terms of closeness of reconstructed distributions to the truth level, there is no  
71 significant difference between 5 cm×5 cm, 2 cm×2 cm and 1 cm×1 cm choices. Both  
72 the ATLAS and CMS detectors use cell sizes which are close to the nuclear interaction  
73 length of the HCAL cells.

#### 74 4. Study of detector performance with soft drop mass

75 In this section, we use the jet mass computed with a specific algorithm, soft drop  
76 declustering, to study the performance of detector with various detector cell sizes and  
77 center-of-mass (c.m.) energies.

##### 78 4.1. The technique of soft drop declustering

79 The soft drop declustering [19] is a grooming method that removes soft wide-  
80 angle radiation from a jet. The constituents of a jet  $j_0$  are first reclustered using  
81 the Cambridge-Aachen (C/A) algorithm [20, 21]. Then, the jet  $j_0$  is broken into two  
82 subjets  $j_1$  and  $j_2$  by undoing the last stage of C/A clustering. If the subjets pass  
83 the following soft drop condition, jet  $j_0$  is the final soft-drop jet. Otherwise, the algo-  
84 rithm redefines  $j_0$  to be the subjet with larger  $p_T$  (among  $j_1$  and  $j_2$ ) and iterates the  
85 procedure.

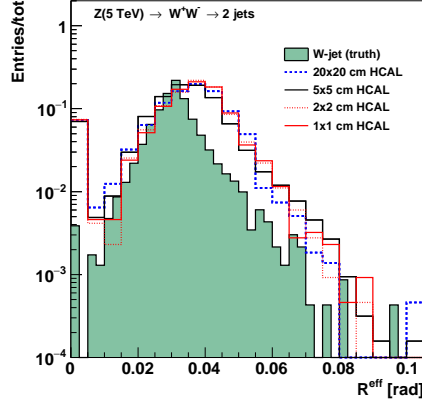
$$\frac{\min(p_{T1}, p_{T2})}{p_{T1} + p_{T2}} > z_{\text{cut}} \left( \frac{\Delta R_{12}}{R_0} \right)^\beta, \quad (1)$$

86 where  $p_{T1}$  and  $p_{T2}$  are the transverse momenta of the two subjets,  $z_{\text{cut}}$  is soft drop  
87 threshold,  $\Delta R_{12}$  is the distance between the two subjets in the rapidity-azimuth angle  
88 plane ( $y-\phi$ ),  $R_0$  is the characteristic radius of the original jet, and  $\beta$  is the angular  
89 exponent.

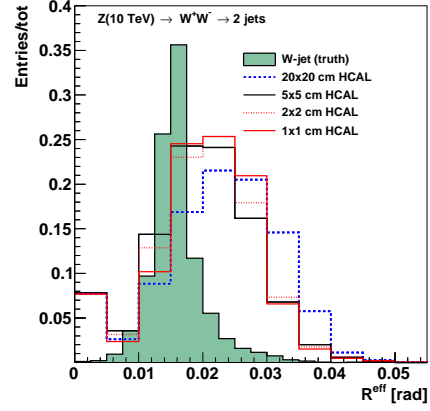
90 In our study, we compare the performance of future detector when setting  $\beta = 0$   
91 versus when setting  $\beta = 2$ . For  $\beta = 0$ , the soft drop condition depends only on the  $z_{\text{cut}}$ .  
92 For  $\beta = 2$ , the condition depends on the angular distance between the two subjets and  
93  $z_{\text{cut}}$  and the algorithm becomes infrared and collinear safe.

##### 94 4.2. Analysis method

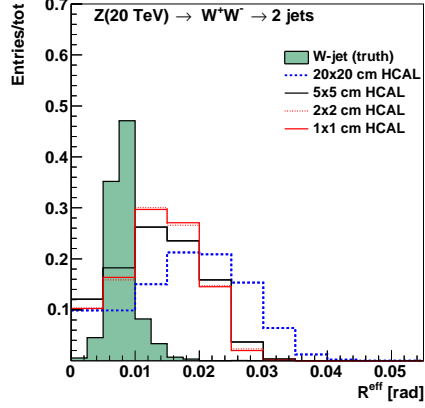
95 We employ the following method to quantify the detector performance and find out  
96 the cell size that gives the best separation power to distinguish signal from background.  
97 For each configuration of detector and c.m. energy, we draw the receiver operating  
98 characteristic (ROC) curves in which the x-axis is the signal efficiency ( $\epsilon_{\text{sig}}$ ) and y-axis



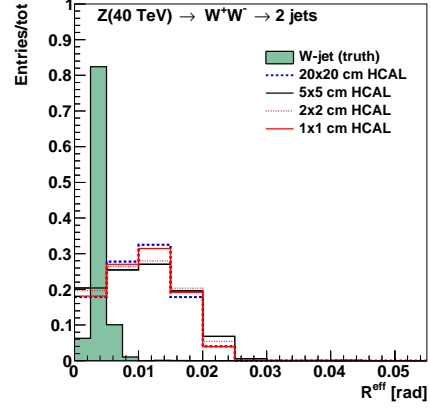
(a) 5 TeV



(b) 10 TeV

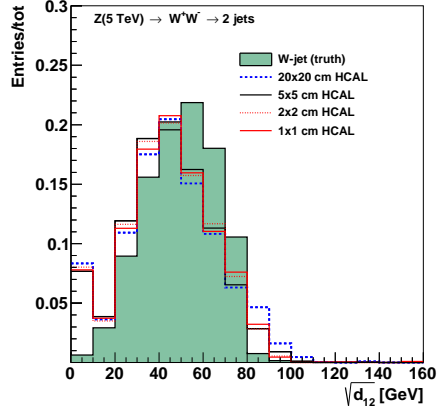


(c) 20 TeV

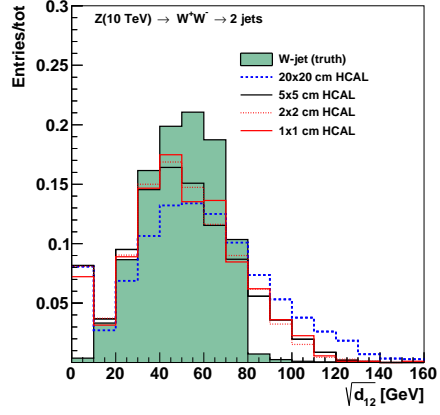


(d) 40 TeV

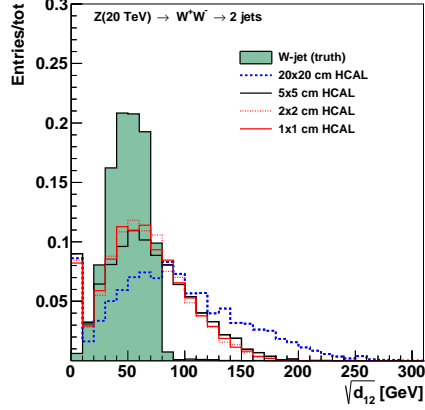
Figure 1: Jet effective radius for different jet transverse momenta and HCAL granularities.



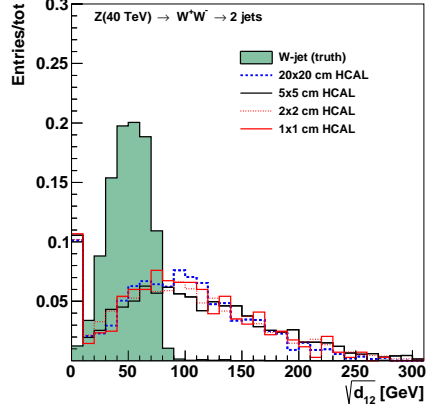
(a) 5 TeV



(b) 10 TeV



(c) 20 TeV



(d) 40 TeV

Figure 2: Jet splitting scale for different jet transverse momenta and HCAL granularity.

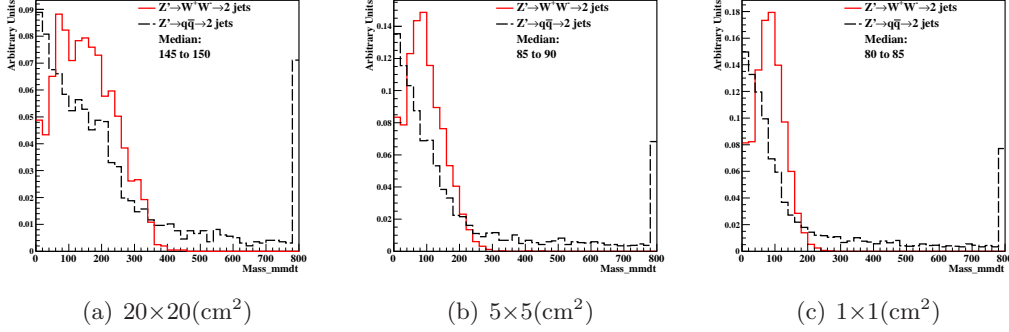


Figure 3: Distributions of soft drop mass for  $\beta=0$ , with 20 TeV c.m. energies and three different detector cell sizes:  $20 \times 20$ ,  $5 \times 5$ , and  $1 \times 1$  ( $\text{cm}^2$ ). The signal (background) process is  $Z' \rightarrow WW$  ( $Z' \rightarrow q\bar{q}$ ).

99 is the inverse of background efficiency ( $1/\epsilon_{\text{bkg}}$ ). In order to scan the efficiencies of soft  
100 drop mass cuts, we vary the mass window as follows. We first look for the median  
101 bin  $i_{\text{med}}^1$  of the soft drop mass histogram from simulated signal events. Taking the  
102 right boundary of bin  $i_{\text{med}}$  as the center of mass window  $x_{\text{center}}$ , we start increasing the  
103 width of mass window symmetrically on the left and on the right of  $x_{\text{center}}$ , in steps of  
104 5 GeV, i.e. the narrowest mass window is  $[x_{\text{center}} - 5, x_{\text{center}} + 5]$ . If one side reaches  
105 the boundary of the mass histogram, we only increase the width on the other side, also  
106 in steps of 5 GeV. For each mass window, there will be corresponding  $\epsilon_{\text{sig}}$  and  $\epsilon_{\text{bkg}}$ ,  
107 which gives a point in the ROC curves.

#### 108 4.3. Results and conclusion

109 Figures 3, 5, 7, and 9 show a few representative distributions for the soft drop mass  
110 for  $\beta = 0$  and  $\beta = 2$  with different c.m. energies and detector cell sizes; the signals  
111 considered are  $Z' \rightarrow WW$  and  $Z' \rightarrow t\bar{t}$ .

112 Figures 4, 6, 8, and 10 show the ROC curves for different detector cell sizes and  
113 c.m. energies.

114 These studies show that the reconstruction of soft drop mass improves with decrease  
115 of the HCAL cell sizes. Figures 4 and 6 show that for  $\beta = 0$  the smallest detector cell  
116 size,  $1 \text{ cm} \times 1 \text{ cm}$ , has the best separation power at  $\sqrt{s} = 5, 10$ , and 20 TeV when the  
117 signal is  $Z' \rightarrow WW$  and at  $\sqrt{s} = 10$  and 20 TeV when the signal is  $Z' \rightarrow t\bar{t}$ . On the  
118 contrary, Figs. 8 and 10 show that for  $\beta = 2$  the smallest detector cell size does not  
119 have improvements in the separation power with respect to those with larger cell sizes.  
120 In fact, the performances of the three cell sizes are similar. In addition, sometimes  
121 bigger detector cell sizes,  $5 \text{ cm} \times 5 \text{ cm}$  or  $20 \text{ cm} \times 20 \text{ cm}$  have the best separation power.

122 We also find that the soft drop mass with  $\beta = 0$  has better performance for distin-  
123 guishing signal from background than for  $\beta = 2$ . Therefore, we will apply requirements  
124 on this variable when studying the other jet substructure variables.

<sup>1</sup>The integral from bin 0 to bin  $i_{\text{med}}$  ( $i_{\text{med}} - 1$ ) should be greater (less) than half of the total number of events. Note, the bin width is 5 GeV.

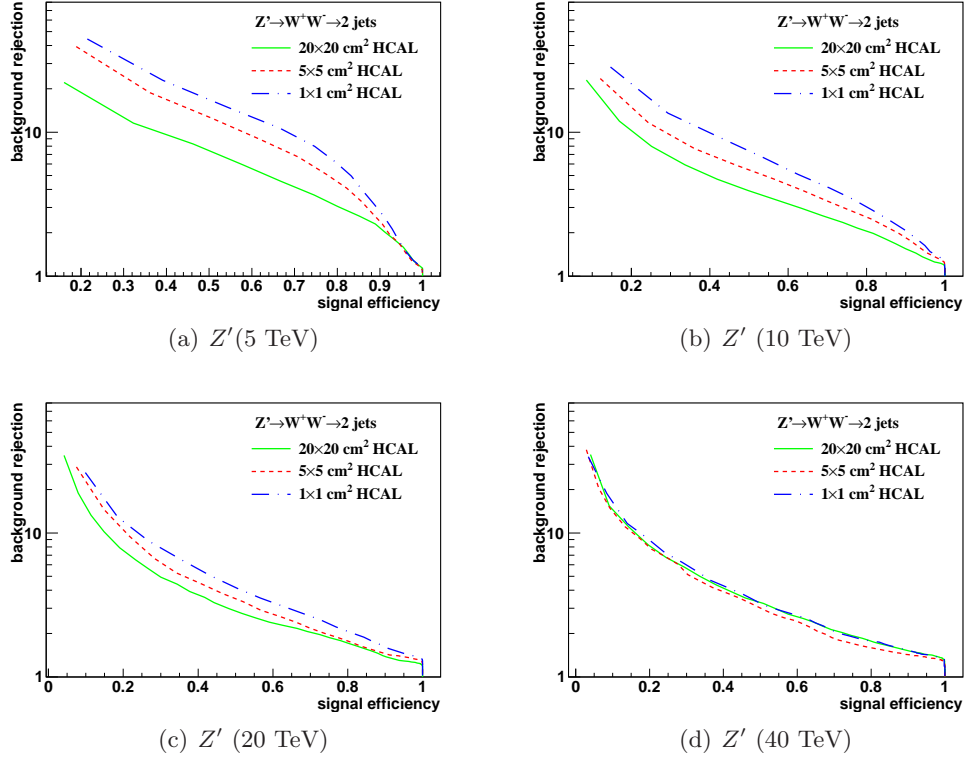


Figure 4: The ROC curves of soft drop mass selection for  $\beta=0$  with 5, 10, 20, 40 TeV c.m. energies. Three different detector cell sizes are compared:  $20\times 20$ ,  $5\times 5$ , and  $1\times 1$  ( $\text{cm}^2$ ). The signal (background) process is  $Z' \rightarrow WW$  ( $Z' \rightarrow q\bar{q}$ ).

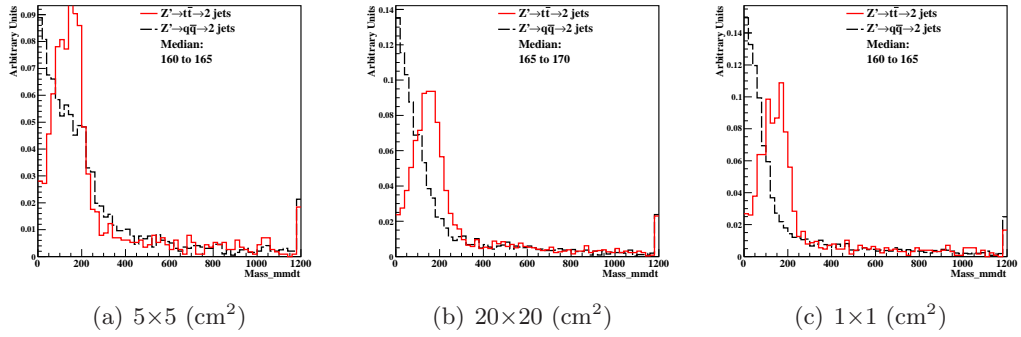


Figure 5: Distributions of soft drop mass for  $\beta=0$ , with 20 TeV c.m. energies and three different detector cell sizes:  $20\times 20$ ,  $5\times 5$ , and  $1\times 1$  ( $\text{cm}^2$ ). The signal (background) process is  $Z' \rightarrow t\bar{t}$  ( $Z' \rightarrow q\bar{q}$ ).

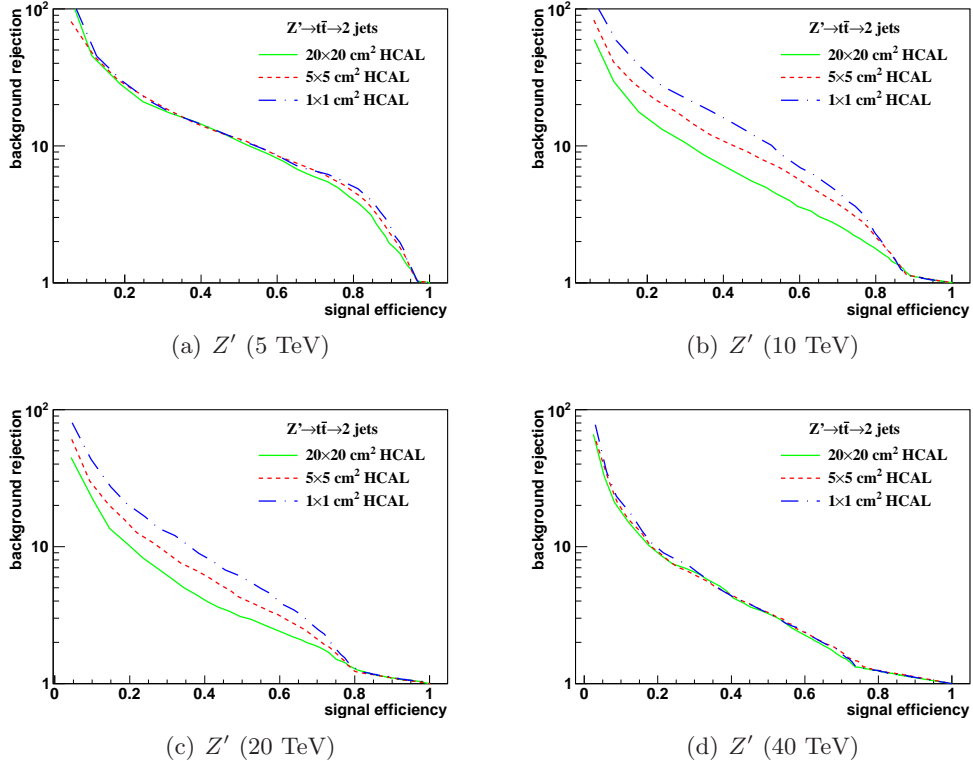


Figure 6: The ROC curves of soft drop mass selection for  $\beta=0$  with 5,10, 20, 40 TeV c.m. energies. Three different detector cell sizes are compared:  $20\times 20$ ,  $5\times 5$ , and  $1\times 1$  ( $\text{cm}^2$ ). The signal (background) process is  $Z' \rightarrow t\bar{t}$  ( $Z' \rightarrow q\bar{q}$ ).

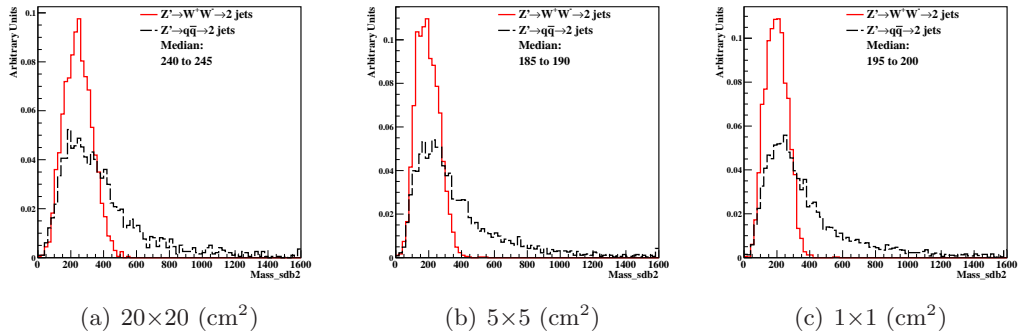


Figure 7: Distributions of soft drop mass for  $\beta=2$ , with 20 TeV c.m. energies and three different detector cell sizes:  $20\times 20$ ,  $5\times 5$ , and  $1\times 1$  ( $\text{cm}^2$ ). The signal (background) process is  $Z' \rightarrow WW$  ( $Z' \rightarrow q\bar{q}$ ).



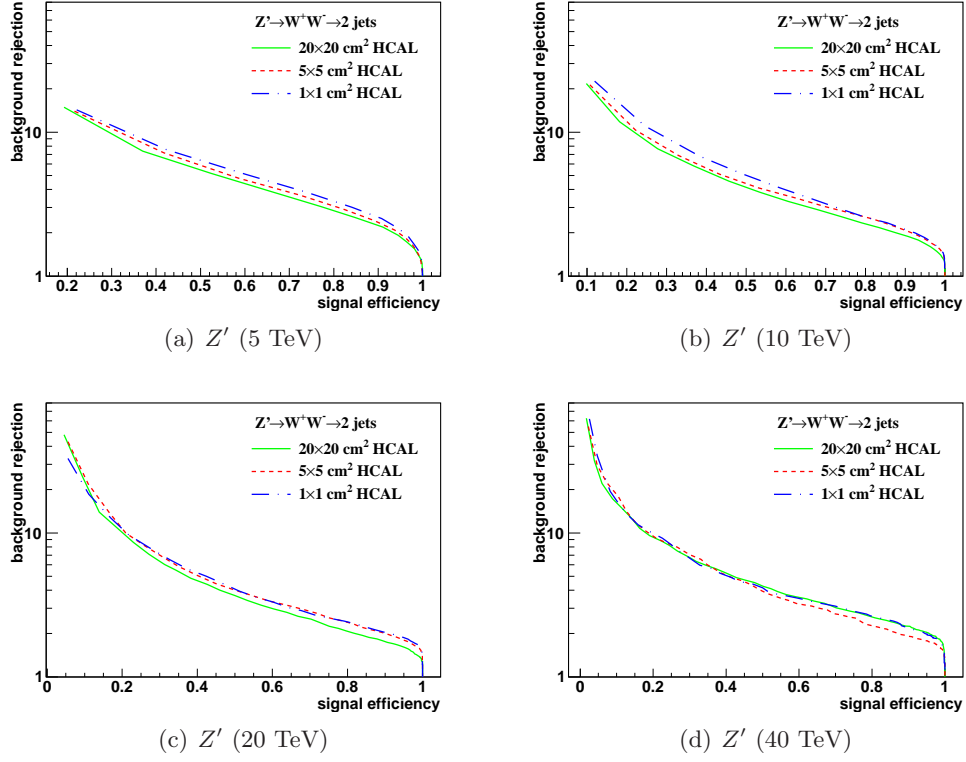


Figure 8: The ROC curves of soft drop mass selection for  $\beta=2$  with 5, 10, 20, 40 TeV c.m. energies. Three different detector cell sizes are compared:  $20\times 20$ ,  $5\times 5$ , and  $1\times 1$  ( $\text{cm}^2$ ). The signal (background) process is  $Z' \rightarrow WW$  ( $Z' \rightarrow q\bar{q}$ ).

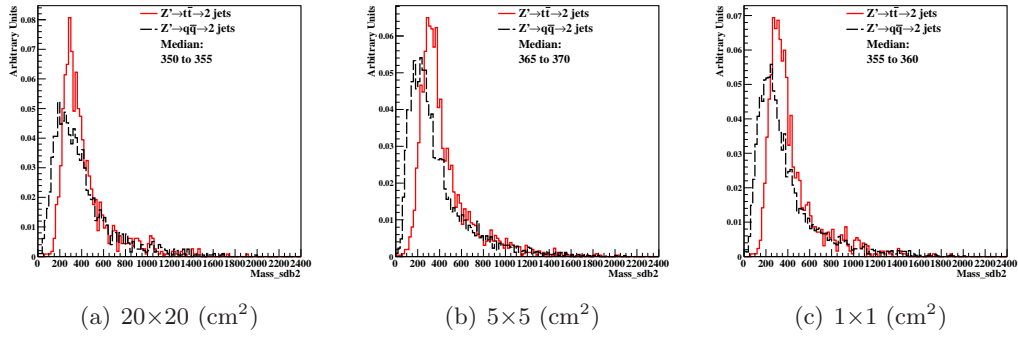


Figure 9: Distributions of soft drop mass for  $\beta=2$ , with 20 TeV c.m. energies and three different detector cell sizes:  $20\times 20$ ,  $5\times 5$ , and  $1\times 1$  ( $\text{cm}^2$ ). The signal (background) process is  $Z' \rightarrow t\bar{t}$  ( $Z' \rightarrow q\bar{q}$ ).

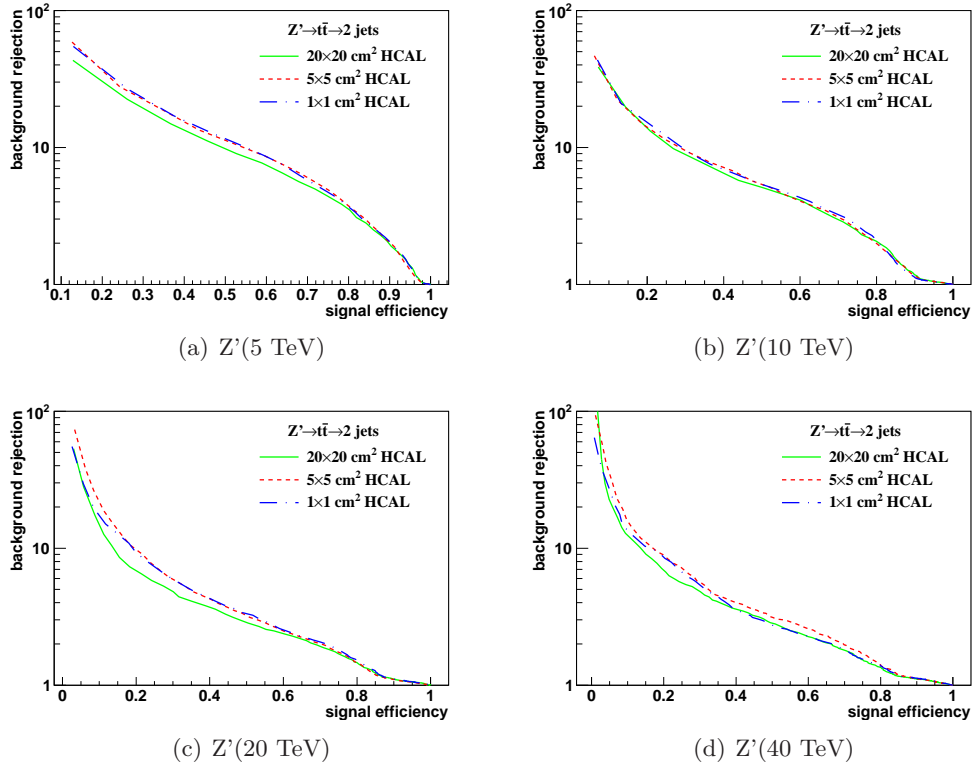


Figure 10: The ROC curves of soft drop mass selection for  $\beta=2$  with 5, 10, 20, 40 TeV c.m. energies. Three different detector cell sizes are compared:  $20 \times 20$ ,  $5 \times 5$ , and  $1 \times 1 \text{ (cm}^2\text{)}$ . The signal (background) process is  $Z' \rightarrow t\bar{t}$  ( $Z' \rightarrow q\bar{q}$ ).

## 5. Study of detector performance with jet substructure variables

In this section, we use several jet substructure variables to study the performance of detector with various detector cell sizes and c.m. energies.

### 5.1. $N$ -subjettiness

The variable  $N$ -subjettiness [22], denoted by  $\tau_N$ , is designed to “count” the number of subjet(s) in a large radius jet so to separate signal jets from decays of heavy bosons and background jets from QCD processes. The  $\tau_N$  is the  $p_T$ -weighted angular distance between each jet constituent and the closest subjet axis:

$$\tau_N = \frac{1}{d_0} \sum_k p_{T,k} \min\{\Delta R_{1,k}, \Delta R_{2,k}, \dots, \Delta R_{N,k}\}, \quad (2)$$

with a normalization factor  $d_0$ :

$$d_0 = \sum_k p_{T,k} R_0.$$

The  $k$  runs over all constituent particles in a given large radius jet,  $p_{T,k}$  is the transverse momentum of each individual constituent particle,  $\Delta R_{j,k} = \sqrt{(\Delta y)^2 + (\Delta \phi)^2}$  is the distance between the constituent particle  $k$  and the candidate subjet axis  $j$  in the  $y - \phi$  plane. The  $R_0$  is the characteristic jet radius used in the anti- $k_t$  jet algorithm.

In this analysis, the anti- $k_t$  algorithm with  $R = 0.4$  (AK4) is first employed to reconstruct jets. The subjet axes are obtained by running the exclusive  $k_t$  algorithm [23] and reversing the last  $N$  clustering steps. Namely, when  $\tau_N$  is computed, the  $k_t$  algorithm is forced to return exactly  $N$  jets. If a large radius jet has  $N$  subjet(s), its  $\tau_N$  is smaller than  $\tau_{N-1}$ . Therefore, in our analysis, the ratio of the  $\tau_N$  variables,  $\tau_{21}$  ( $\tau_2/\tau_1$ ) and  $\tau_{32}$  ( $\tau_3/\tau_2$ ), are used to distinguish the one-prong background jets and the two-prong jets from  $W$  or the three-prong jets from  $top$ .

We use the ROC curves as described in Section 4.2 to analyze the detector performance and determine the cell size that gives the best separation power to distinguish signal from background. Following the suggestion by Ref. [24], requirement on the soft drop mass with  $\beta = 0$  is applied before the study of  $N$ -subjettiness. For each detector configuration and c.m. energy, the soft drop mass selection is determined as follows. First, we look for the median bin of the soft drop mass histogram from simulated signal events as described in Section 4.2. Then, we compare the numbers of events in the bins adjacent to the medium bin (bin  $i_{\text{med}} - 1$  and bin  $i_{\text{med}} + 1$ ). The bin with larger number of events is added, in addition to the medium bin, to extend the mass window. The procedure is repeated until the window contains at least 75% of the total number of signal events.

In order to obtain the signal and background efficiencies, various ranges of the  $\tau_{21}$  and  $\tau_{32}$  are scanned. Since some of the background distributions have long tails and leak into the signal-dominated region, we use the following method as suggested by the Pearson Lemma Method to determine the ranges of  $\tau$  variables. First, we take the ratio of the signal to background  $\tau_{21}$  ( $\tau_{32}$ ) histograms. The boundaries of the bin (seed bin) with maximum signal to background ratio (S/N) give us the first range of  $\tau$  selection:

162  $x_{\text{low}}^{\text{seedbin}} < \tau_{21} < x_{\text{high}}^{\text{seedbin}}$ . Then, we compare the S/N in the bins adjacent to the seed  
 163 bin. The bin with larger S/N is added, in addition to the seed bin, to extend the  $\tau_{21}$   
 164 selection window. Every window has its corresponding  $\epsilon_{\text{sig}}$  and  $1/\epsilon_{\text{bkg}}$  and an ROC  
 165 curve is mapped out.

166 In addition to the ROC curves, we use the so-called "Mann-Whitney" test to quan-  
 167 tify the detector performance. The value of Mann-Whitney is related to the integrated  
 168 area under the ROC curve: if the value is bigger, it indicates the signal and background  
 169 distributions have similar shapes and can not be well separated from each other. Vice  
 170 versa, if the value is smaller, we can achieve a better signal and background separation.

171 Figures 11 and 13 show the distributions of  $\tau_{21}$  and  $\tau_{32}$  for  $\sqrt{s} = 20$  TeV after  
 172 applying requirement on the soft drop mass. The signals considered are  $Z' \rightarrow WW$  ( $\tau_{21}$ )  
 173 and  $Z' \rightarrow t\bar{t}$  ( $\tau_{32}$ ). Figures 12 and 14 present the ROC curves from different detector  
 174 cell sizes and c.m. energies, respectively. The smallest detector cell size ( $1 \times 1 \text{ cm}^2$ )  
 175 does not have the best separation power. In fact, in some cases, the best separation  
 176 power comes from detector with bigger cell sizes ( $5 \times 5 \text{ cm}^2$  and  $20 \times 20 \text{ cm}^2$ ).

177 Figures 17 (a) and (b) present the summary plots of  $\tau_{21}$  and  $\tau_{32}$  with various detector  
 178 cell sizes and c.m. energies using Mann Whitney U test. For  $\tau_{21}$  at smaller c.m.  
 179 energies, when cell size is smaller, the detector performance improves. However, when  
 180 c.m. energy increases, no improvement is observed using the smallest detector cell size  
 181 ( $1 \times 1 \text{ cm}^2$ ). For  $\tau_{32}$ , the case is similar to  $\tau_{21}$ . Even worse, with some c.m. energies,  
 182 the bigger detector cell sizes ( $5 \times 5 \text{ cm}^2$  and  $20 \times 20 \text{ cm}^2$ ) have better separation power  
 183 than the smallest detector size.

## 184 5.2. Energy correlation function

185 The energy correlation function (ECF) [25] is defined as follows:

$$ECF(N, \beta) = \sum_{i_1 < i_2 < \dots < i_N \in J} \left( \prod_{a=1}^N p_{Tia} \right) \left( \prod_{b=1}^{N-1} \prod_{c=b+1}^N R_{i_b i_c} \right)^\beta, \quad (3)$$

186 where the sum is looped all particles in the jet  $J$ ,  $p_T$  is the transverse momentum of  
 187 each individual particle, and  $R$  is the distance between two particles in the  $y$ - $\phi$  plane.  
 188 In order to use a dimensionless variable, a parameter  $r_N$  is defined:

$$r_N^{(\beta)} \equiv \frac{ECF(N+1, \beta)}{ECF(N, \beta)}. \quad (4)$$

189 The idea of  $r_N$  comes from N-subjettiness  $\tau_N$ . Both  $r_N$  and  $\tau_N$  are linear in the  
 190 energy of the soft radiation for a system of  $N$  partons with soft radiation. In gen-  
 191 eral, if the system has  $N$  subjets,  $ECF(N+1, \beta)$  should be significantly smaller than  
 192  $ECF(N, \beta)$ . Therefore, we can use this feature to distinguish jets with different num-  
 193 ber of subjets. As in Section 5.1, the ratio  $r_N/r_{N-1}$ , denoted by  $C_N$ , (double ratios of  
 194 ECFs) is used to study the detector performance:

$$C_N^{(\beta)} \equiv \frac{r_N^{(\beta)}}{r_{N-1}^{(\beta)}} = \frac{ECF(N-1, \beta) ECF(N+1, \beta)}{ECF(N, \beta)^2}. \quad (5)$$

195 In our analysis, we set  $N = 2$  and  $\beta = 1$  ( $C_2^1$ ).

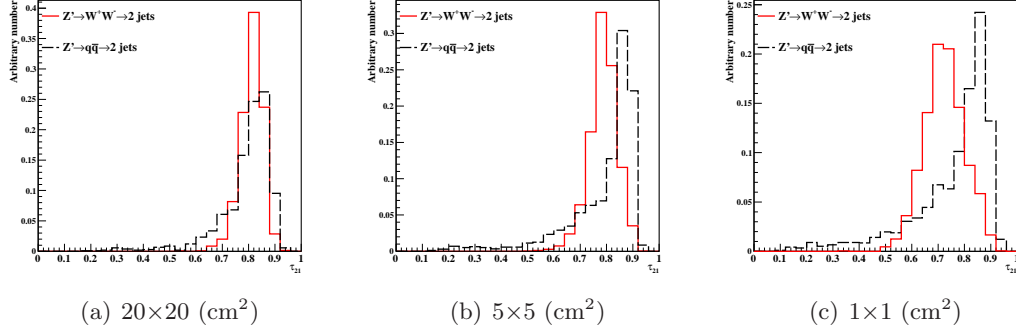


Figure 11: Distributions of  $\tau_{21}$  in 20 TeV energy collision for different detector sizes. Cell sizes in  $20 \times 20$ ,  $5 \times 5$ , and  $1 \times 1$   $\text{cm}^2$  are shown here.

Figure 15 presents the histograms of  $C_2^1$  with  $\sqrt{s} = 20$  TeV after making requirement on the soft drop mass. The signal considered is  $Z' \rightarrow WW$ . Figure 16 shows the ROC curves from different detector cell sizes for each c.m. energy, respectively. One can see that the smallest detector cell size ( $1 \times 1$   $\text{cm}^2$ ) does not have the best signal/background separation power. Figure 17(c) summarizes the result of the Mann Whitney U test for  $C_2^1$ . When c.m. energy increases, no improvement is observed from detector with the smallest cell size.

## 6. Conclusions

The studies presented in this paper show that the reconstruction of jet substructure variables for future particle colliders will benefit from small cell sizes of the hadronic calorimeters. This conclusion was obtained using the realistic Geant4 simulation of calorimeter responses combined with reconstruction of calorimeter clusters used as inputs for jet reconstruction. Hadronic calorimeters that use the cell sizes of  $20 \times 20$   $\text{cm}^2$  are least performant almost for every substructure variables considered in this analysis for jet transverse momenta between 2.5 to 10 TeV. Such cell sizes are close to the nuclear interaction length of the considered calorimeter, and are similar to those used for the ATLAS and CMS detectors. The performance of hadronic calorimeters with  $2 \times 2$   $\text{cm}^2$  and  $1 \times 1$   $\text{cm}^2$  cells are found to be similar.

It is however interesting to note that, for very boosted jets with transverse momenta close to 20 TeV, no significant improvement with the decrease of cell sizes was observed. This result needs to be understood in terms of various type of simulations and different options for construction of the calorimeter clusters.

## Acknowledgements

This research was performed using resources provided by the Open Science Grid, which is supported by the National Science Foundation and the U.S. Department of Energy's Office of Science. We gratefully acknowledge the computing resources provided on Blues, a high-performance computing cluster operated by the Laboratory Computing Resource Center at Argonne National Laboratory. Argonne National Laboratory's

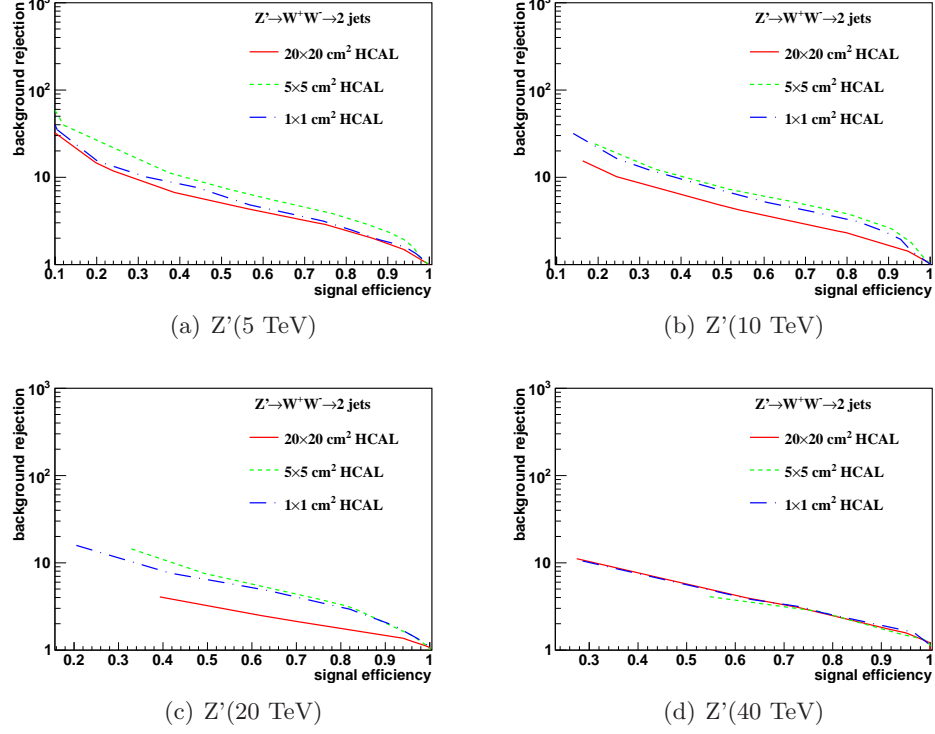


Figure 12: Signal efficiency versus background rejection rate using  $\tau_{21}$ . The energies of collision at (a) 5, (b) 10, (c) 20, and (d) 40 TeV are shown here. In each figure, the three ROC curves correspond to different detector sizes.

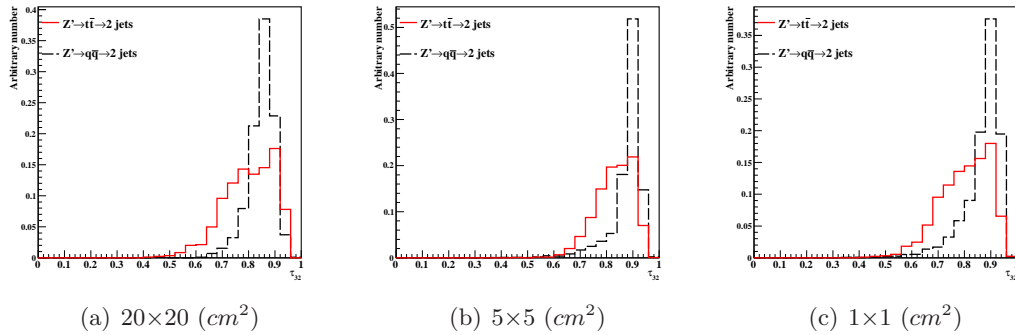


Figure 13: Distributions of  $\tau_{32}$  in 20 TeV energy collision for different detector sizes. Cell sizes in  $20 \times 20$ ,  $5 \times 5$ , and  $1 \times 1 \text{ cm}^2$  are shown here.

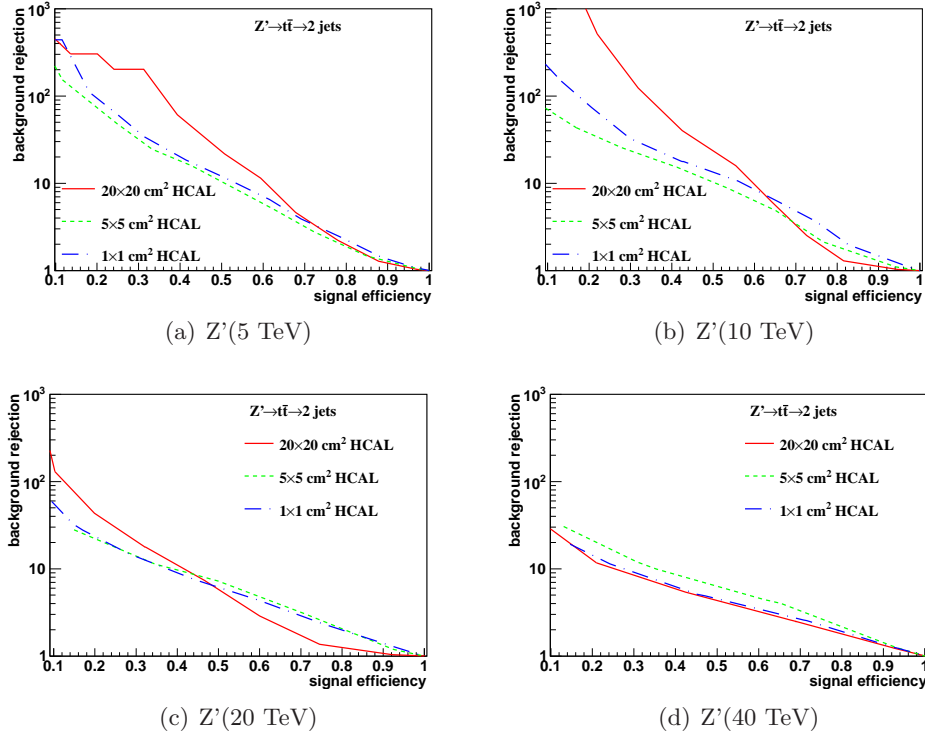


Figure 14: Signal efficiency versus background rejection rate using  $\tau_{32}$ . The energies of collision at (a) 5, (b) 10, (c) 20, and (d) 40 TeV are shown here. In each figure, the three ROC curves correspond to different detector sizes.

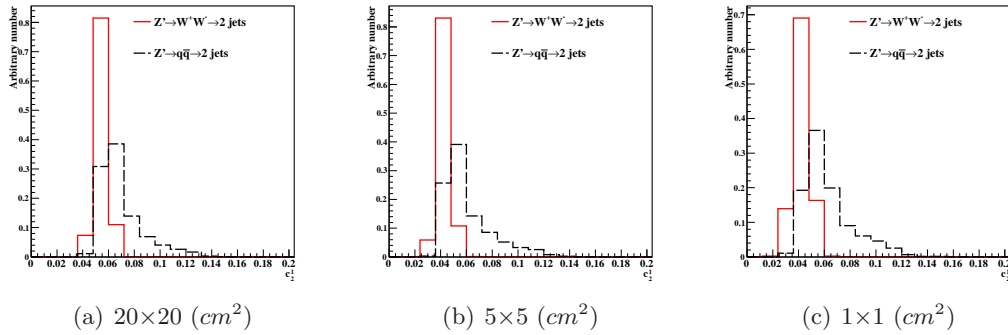


Figure 15: Distributions of  $C_2^1$  in 20 TeV energy collision for different detector sizes. Cell sizes in  $20 \times 20$ ,  $5 \times 5$ , and  $1 \times 1 \text{ cm}^2$  are shown here.

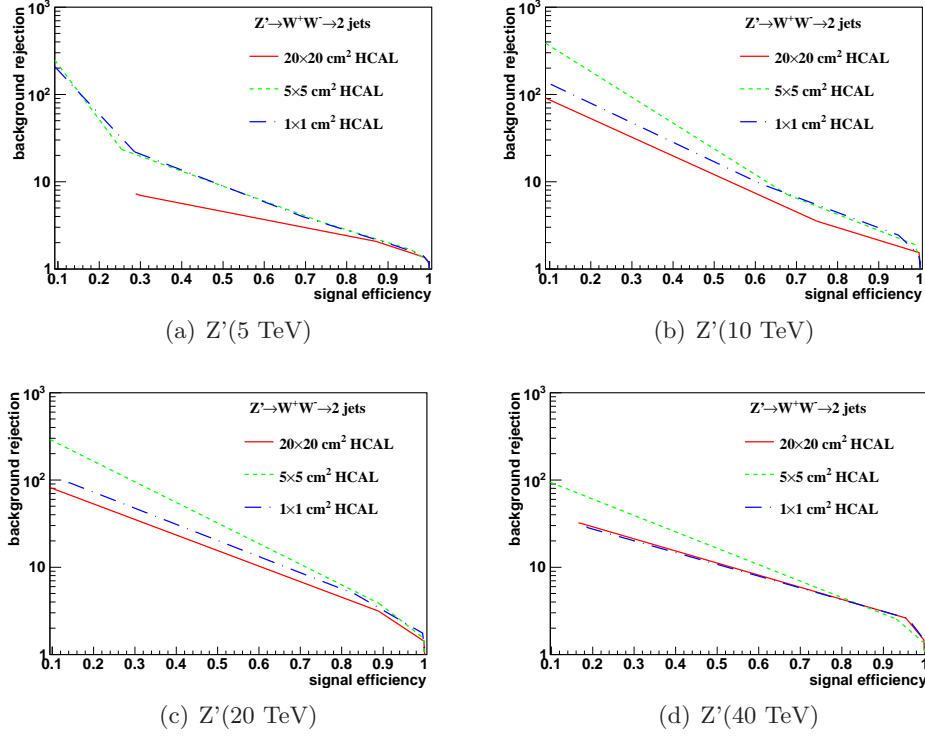


Figure 16: Signal efficiency versus background rejection rate using  $C_2^{(1)}$ . The energies of collision at (a) 5, (b) 10, (c) 20, and (d) 40 TeV are shown here. In each figure, the three ROC curves correspond to different detector sizes.

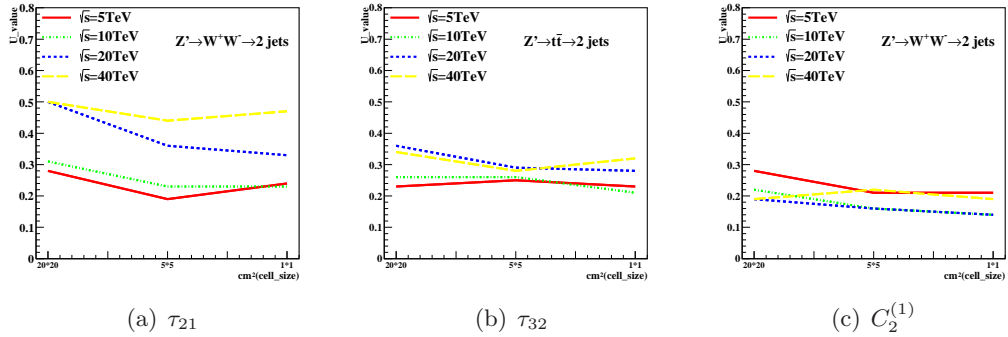


Figure 17: The Mann-Whitney U values for  $\tau_{21}$ ,  $\tau_{32}$ , and  $C_2^{(1)}$  reconstructed with different collision energies and detector cell sizes.



224 work was supported by the U.S. Department of Energy, Office of Science under con-  
225 tract DE-AC02-06CH11357. The Fermi National Accelerator Laboratory (Fermilab) is  
226 operated by Fermi Research Alliance, LLC under Contract No. DE-AC02-07CH11359  
227 with the United States Department of Energy.

## 228 References

- 229 [1] M. Benedikt, [The Global Future Circular Colliders Effort](#) CERN-ACC-SLIDES-2016-0016. Pre-  
230 sented at P5 Workshop on the Future of High Energy Physics, BNL, USA, Dec. 15-18, 2013.  
231 URL <http://cds.cern.ch/record/2206376>
- 232 [2] J. Tang, et al., Concept for a Future Super Proton-Proton Collider (2015). [arXiv:1507.03224](#).
- 233 [3] R. Calkins, et al., [Reconstructing top quarks at the upgraded LHC and at future accelerators](#), in:  
234 Proceedings, Community Summer Study 2013: Snowmass on the Mississippi (CSS2013): Min-  
235 neapolis, MN, USA, July 29-August 6, 2013. [arXiv:1307.6908](#).  
236 URL <https://inspirehep.net/record/1244676/files/arXiv:1307.6908.pdf>
- 237 [4] S. V. Chekanov, J. Dull, Energy range of hadronic calorimeter towers and cells for high-pT jets  
238 at a 100 TeV collider <http://arxiv.org/abs/1511.01468> [arXiv:1511.01468](#).
- 239 [5] E. Coleman, M. Freytsis, A. Hinzmann, M. Narain, J. Thaler, N. Tran, C. Vernieri, The importance  
240 of calorimetry for highly-boosted jet substructure [arXiv:1709.08705](#).
- 241 [6] DELPHES 3 Collaboration, J. de Favereau, C. Delaere, P. Demin, A. Giammanco, V. Lematre,  
242 A. Mertens, M. Selvaggi, DELPHES 3, A modular framework for fast simulation of a generic  
243 collider experiment, JHEP 02 (2014) 057. [arXiv:1307.6346](#), [doi:10.1007/JHEP02\(2014\)057](#).
- 244 [7] S. V. Chekanov, M. Beydler, A. V. Kotwal, L. Gray, S. Sen, N. V. Tran, S. S. Yu, J. Zuzelski, Initial  
245 performance studies of a general-purpose detector for multi-TeV physics at a 100 TeV pp collider,  
246 JINST 12 (06) (2017) P06009. [arXiv:1612.07291](#), [doi:10.1088/1748-0221/12/06/P06009](#).
- 247 [8] J. Allison, et al., Recent developments in Geant4, Nuclear Instruments and Methods in Physics  
248 Research A 835 (2016) 186.
- 249 [9] M. J. Charles, PFA Performance for SiD, in: Linear colliders. Proceedings, International Linear  
250 Collider Workshop, LCWS08, and International Linear Collider Meeting, ILC08, Chicago, USA,  
251 November 16-20, 2008 , 2009. [arXiv:0901.4670](#).
- 252 [10] J. S. Marshall, M. A. Thomson, Pandora Particle Flow Algorithm, in: Proceedings, Interna-  
253 tional Conference on Calorimetry for the High Energy Frontier (CHEF 2013), 2013, pp. 305–315.  
254 [arXiv:1308.4537](#).
- 255 [11] G. P. S. M. Cacciari, G. Soyez, FastJet user manual CERN-PH-TH/2011-297. [arXiv:1111.6097](#).
- 256 [12] M. Cacciari, G. P. Salam, G. Soyez, The anti-kt jet clustering algorithm, JHEP 0804 (2008) 063.  
257 [arXiv:0802.1189](#).
- 258 [13] S. Chekanov, HepSim: a repository with predictions for high-energy physics experiments, Advances  
259 in High Energy Physics 2015 (2015) 136093, available as <http://atlaswww.hep.anl.gov/hepsim/>.
- 260 [14] B. Auerbach, S. Chekanov, J. Love, J. Proudfoot, A. Kotwal, Sensitivity to new high-mass states  
261 decaying to  $t\bar{t}b\bar{a}$  at a 100 TeV collider <http://arxiv.org/abs/1412.5951> [arXiv:1412.5951](#).
- 262 [15] J. Butterworth, B. Cox, J. R. Forshaw,  $WW$  scattering at the CERN LHC, Phys.Rev. D65 (2002)  
263 096014. [arXiv:hep-ph/0201098](#), <http://dx.doi.org/10.1103/PhysRevD.65.096014> [doi:10.1103/](#)  
264 [PhysRevD.65.096014](#).
- 265 [16] S. Catani, Y. L. Dokshitzer, M. H. Seymour, B. R. Webber,  
266 [Longitudinally-invariant k-clustering algorithms for hadron-hadron collisions](#), Nuclear Physics B  
267 406 (12) (1993) 187 – 224.  
268 URL <http://www.sciencedirect.com/science/article/pii/055032139390166M>
- 269 [17] S. D. Ellis, D. E. Soper, Successive combination jet algorithm for hadron collisions, Phys. Rev. D48  
270 (1993) 3160–3166. [arXiv:hep-ph/9305266](#), <http://dx.doi.org/10.1103/PhysRevD.48.3160> [doi:](#)  
271 [10.1103/PhysRevD.48.3160](#).
- 272 [18] ATLAS Collaboration Collaboration, G. Aad, et al., Jet mass and substructure of inclusive jets in  
273  $\sqrt{s} = 7$  TeV  $pp$  collisions with the ATLAS experiment, JHEP 1205 (2012) 128. [arXiv:1203.4606](#),  
274 [doi:10.1007/JHEP05\(2012\)128](#).
- 275 [19] A. J. Larkoski, S. Marzani, G. Soyez, J. Thaler, Soft Drop, JHEP 05 (2014) 146. [arXiv:1402.2657](#),  
276 [doi:10.1007/JHEP05\(2014\)146](#).
- 277 [20] Y. L. Dokshitzer, G. D. Leder, S. Moretti, B. R. Webber, Better jet clustering algorithms, JHEP  
278 08 (1997) 001. [arXiv:hep-ph/9707323](#), <http://dx.doi.org/10.1088/1126-6708/1997/08/001> [doi:](#)  
279 [10.1088/1126-6708/1997/08/001](#).
- 280 [21] M. Wobisch, T. Wengler, Hadronization corrections to jet cross-sections in deep inelastic scattering,  
281 in: Monte Carlo generators for HERA physics. Proceedings, Workshop, Hamburg, Germany, 1998-  
282 1999, 1998, pp. 270–279. [arXiv:hep-ph/9907280](#).

- 283 [22] J. Thaler, K. Van Tilburg, Identifying Boosted Objects with N-subjettiness, JHEP 03 (2011) 015.  
 284 [arXiv:1011.2268](#), [doi:10.1007/JHEP03\(2011\)015](#).
- 285 [23] S. Catani, Y. L. Dokshitzer, M. H. Seymour, B. R. Webber, Longitudinally-invariant  $k_{\perp}$ -clustering  
 286 algorithms for hadron-hadron collisions, Nucl. Phys. B 406 (CERN-TH-6775-93. LU-TP-93-2)  
 287 (1993) 187–224.
- 288 [24] F. A. Dreyer, L. Necib, G. Soyez, J. Thaler, Recursive Soft Drop, JHEP 06 (2018) 093.  
 289 [arXiv:1804.03657](#), [doi:10.1007/JHEP06\(2018\)093](#).
- 290 [25] A. J. Larkoski, G. P. Salam, J. Thaler, Energy Correlation Functions for Jet Substructure, JHEP  
 291 06 (2013) 108. [arXiv:1305.0007](#), [doi:10.1007/JHEP06\(2013\)108](#).